



# Grain growth and second-phase precipitation in nanocrystalline aluminum–manganese electrodeposits

Ting-Yun Huang<sup>1</sup>, Arvind R. Kalidindi<sup>1</sup>, and Christopher A. Schuh<sup>1,\*</sup>

<sup>1</sup>Department of Materials Science and Engineering, Massachusetts Institute of Technology, 77 Massachusetts Avenue, Cambridge, MA 02139, USA

Received: 29 July 2017

Accepted: 26 October 2017

Published online:

2 November 2017

© Springer Science+Business Media, LLC 2017

## ABSTRACT

The structural stability of nanocrystalline aluminum–manganese (Al-6.5 at.% Mn) alloys is studied in the temperature range of 200–400 °C. Transmission electron microscopy shows that grain growth in this alloy is subdued by the presence of Mn, such that 100 nm or finer grain sizes can be retained at 200 and 300 °C even after 1 month of annealing. In contrast, the principal mode of instability in the alloy is the precipitation of the equilibrium Al<sub>6</sub>Mn phase, which was observed to form at much shorter timescales and is present at 300 and 400 °C after just 30 min. Differential scanning calorimetry was used to study the kinetics of the Al<sub>6</sub>Mn reaction using Johnson–Mehl–Avrami–Kolmogorov analysis and construct a time–temperature–transformation (TTT) diagram for this process. It is found that this Al–Mn single-phase nanostructured alloy can be stable against forming the Al<sub>6</sub>Mn phase and against grain growth for several months below 200 °C and for short thermal excursions up to 300 °C.

## Introduction

Conventional aluminum–manganese alloys are widely used for manufacturing foil, roof sheets, cooking utensils, and rigid containers, because of their high ductility, good mechanical strength, and excellent corrosion resistance [1, 2]. Beyond the conventional Al–Mn alloys, it has been suggested that electrodeposition of Al–Mn from room temperature ionic liquids could be a scalable way to produce nanostructured and amorphous alloys in this system,

with superior mechanical properties [3]. In particular, the solid-solution Al(Mn) FCC phase can be deposited with a nanoscale grain size for compositions up to about 8 at.% Mn [4, 5], and this phase can be both very hard and ductile [6]. This combination of properties is useful for applications requiring high specific strength and wear resistance, and the electroforming route is amenable to many product forms including foils, sheets, and thin-section net-shaped parts [6, 7]. For these reasons, in the present work we explore the Al-6.5 at.% Mn alloy specifically, which

Address correspondence to E-mail: schuh@mit.edu

adopts a solid-solution FCC nanocrystalline structure.

However, as with all nanostructured materials, the high proportion of grain boundary area in electrodeposited Al-Mn alloys raises questions of thermal stability. Nanostructured materials can suffer from grain coarsening at relatively low temperatures [8–10], and nanostructured aluminum in particular has been shown to exhibit grain growth from the nanoscale to the microscale when heated above 170 °C within 1 hour [11]. It is not yet established how the presence of Mn affects nanostructure stability in the Al-Mn system. In our recent work [5], we showed with high-resolution transmission electron microscopy and atom probe tomography that the grain boundaries in Al-6.5 at.% Mn are preferentially decorated with excess Mn solute, even in the as-deposited condition. This is a positive attribute of the system: Grain boundary segregation suggests that the grain boundary energy is lowered as compared with an unsegregated boundary, and segregation also should involve attendant solute drag forces that oppose grain boundary motion. On the other hand, Mn enrichment at the boundaries to levels as high as 12.5 at.% places the local composition well beyond the bulk solubility limit of 0.62 at.% and could facilitate decomposition of the system into FCC Al and second-phase intermetallic Al<sub>6</sub>Mn. As with other nanocrystalline alloys such as Ni-P or Ni-W [12–15], the stability against not only grain growth but also phase separation is a question of practical concern for a proposed engineering material.

It is therefore our purpose in this work to explore the structural evolution of nanocrystalline solid-solution Al-6.5 at.% Mn alloys during post-deposition heating. We consider a broad range of times and temperatures, including both short, high-temperature excursions, as would be relevant for post-processing thermal budgets (i.e., for forming, joining, etc.), and long-term stability at lower temperatures, which would be relevant in usage. After first exploring the basic structure of the as-deposited alloys, Al-6.5 at.% Mn samples are subjected to calorimetry and annealing under various conditions to study grain growth and the eventual phase separation into the equilibrium solution-plus-intermetallic structure. The kinetics of the transformation process are analyzed using a Johnson-Mehl-Avrami-Kolmogorov (JMAK)-like kinetic model, and a time-temperature-transformation diagram is developed to guide thermal processing and usage of the alloy.

## Experimental methods

A sheet of electrodeposited Al-Mn alloy was provided by Xtallic Corporation (Marlborough, MA). While the details of the electrodeposition process for this commercial alloy are proprietary to Xtallic Corporation, the general process may be expected to bear some similarities with other electroplating studies of Al-Mn [3–6]. The sheet was received still adhered to a 5 by 5 cm<sup>2</sup> brass panel. The deposit had a thickness of about 300 μm and was removed from the substrate using concentrated nitric acid (79%, Sigma-Aldrich) before being cut into small square specimens of about 25 mm<sup>2</sup> in area for composition measurement using calibrated energy-dispersive spectroscopy (EDS). Some of the specimens cut from the edges exhibited compositions away from the target composition of 6.5 at.% Mn by as much as 1–2 at.%. Accordingly, only specimens with concentrations close to the target of 6.5 ± 0.4 at.% Mn were grouped together for further study in this paper; these generally came from the center of the deposited sheet.

X-ray diffraction (XRD) was conducted using a zero background holder with a PANalytical X'Pert x-ray diffractometer operated at 40 mA and 45 kV with a CuKα source. Phase identification was conducted using Rietveld refinement, with the refinement template calibrated on standard silicon powder 640b, with a slit size of 2°, and a beam size of 4 mm, from 15° to 125° 2θ. The XRD data were used only for phase identification and not for grain size estimation, because although the as-deposited grain size is below 100 nm, and therefore accessible by line broadening measurements, many of the annealed samples had grain sizes beyond the resolution limit available (~ 100 nm) with the present apparatus. Instead, grain size and microstructure were characterized using a JEOL 2010F transmission electron microscope (TEM). TEM samples were prepared by first manually thinning down the freestanding deposited sheet using SiC paper from 400 to 4000 grit and subsequently electrochemically polishing in an etching solution with 5% perchloric acid, 20% butoxyethanol, and 75% methanol at – 20 °C with 25 V and 15 mA using a Fischione twin-jet polisher. The TEM samples were from roughly the middle of the film's thickness. For the measurement of grain size, multiple dark-field images were taken to achieve better contrast between grains, and over 100 grains were counted in

this manner to determine the grain size distribution and average grain size.

Multiple types of annealing tests were conducted. For kinetic studies, at least 1 mg of sample was placed into a TA Discovery differential scanning calorimeter (DSC) to be scanned over the temperature range between 50 and 550 °C at a constant ramping rate ranging from 5 to 15 °C/min, under flowing nitrogen. The slow ramping rate and large amount of sample used were to ensure the heat released during transformation was distinguishable from the background. Selected samples were sealed in glass ampoules under a purified Ar atmosphere and isothermally annealed at 200, 300 and 400 °C for various lengths of time for phase transformation and grain growth studies. The isochronal DSC measurements were used to fit parameters for a kinetic model, as described in the “Kinetic analysis” section. To ensure unbiased curve fitting in determining the model parameters, the background heat flow was subtracted, and the remaining signal curve was interpolated using a custom MATLAB program to make sure that each data set had the same number of evenly spaced data points.

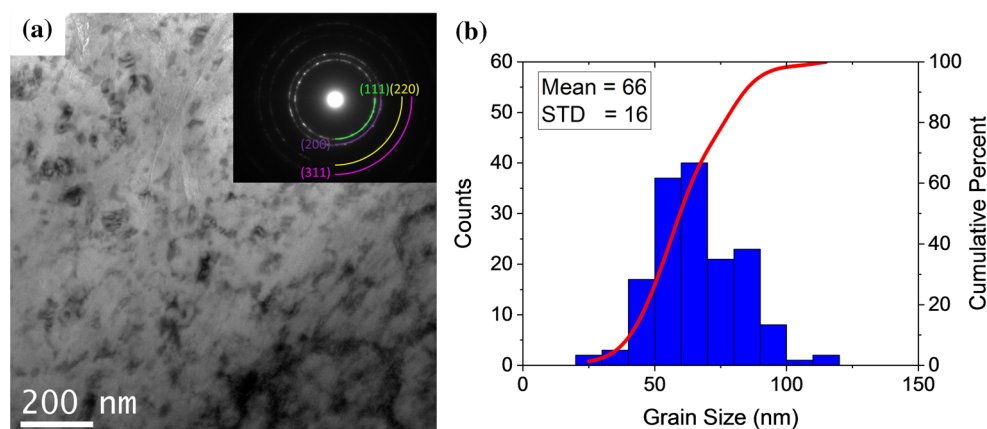
### Grain growth and intermetallic precipitation

Figure 1 shows the structure of the Al-6.5 at.% Mn alloy in the as-deposited condition. The bright-field image in Fig. 1a reveals a grain size that is in the nanocrystalline range, and the inset electron

diffraction pattern identifies a single-phase FCC nanocrystalline solid solution, with the first few diffraction rings indexed as (111), (200), (220) and (311). The grain size statistics for this sample were measured from a series of dark-field images (as described in the “Experimental methods” section) and shown in Fig. 1b. The average grain size is about 66 nm, and the distribution is reasonably tight with a standard deviation of 16 nm. The as-deposited structure also shows evidence of additional structural debris through the mottled appearance of the individual grains and the lack of definition of grain boundaries; this is likely associated with additional defects such as dislocations that are naturally present in the as-deposited condition.

TEM micrographs of samples after annealing at 200, 300, or 400 °C isothermally from 30 min to 1 month are shown in Figs. 2 and 3. Figure 2 focuses on the first few hours of annealing, while Fig. 3 shows results after a month. At 200 °C, the first few hours of annealing lead to a mild coarsening of the grain structure, but the mottled appearance of the grains remains. After 4 h of annealing, the average grain size is around 100 nm, and this appears to be a relatively stable condition as the structure after annealing 1 month at 200 °C, shown in Fig. 3a, does not present substantial additional coarsening. Moreover, the samples annealed at 200 °C do not exhibit any indications of second-phase precipitation, even after 1 month of annealing.

XRD data for these annealed samples are shown in Fig. 4, where the position of the dominant Al<sub>6</sub>Mn peak is denoted with a diamond, and no peak



**Figure 1** **a** A TEM bright field image of the as-deposited Al-Mn alloy, in which the inset electron diffraction pattern exhibits a set of diffraction rings consistent with a single phase solid solution with

fine grains. **b** The grain size distribution measured using dark field images. The average grain size for this particular sample is 66 nm, with a standard deviation of 16 nm.

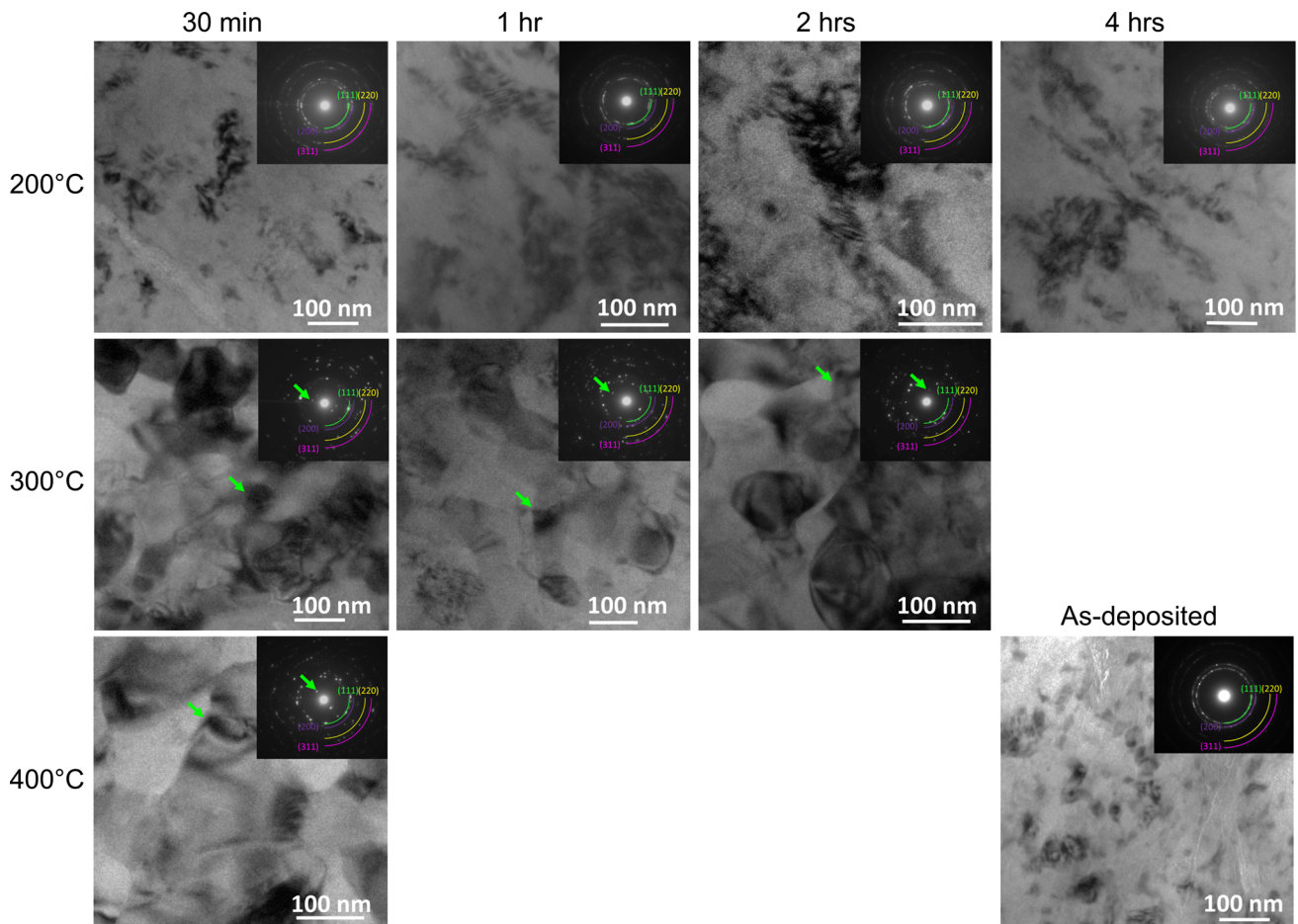
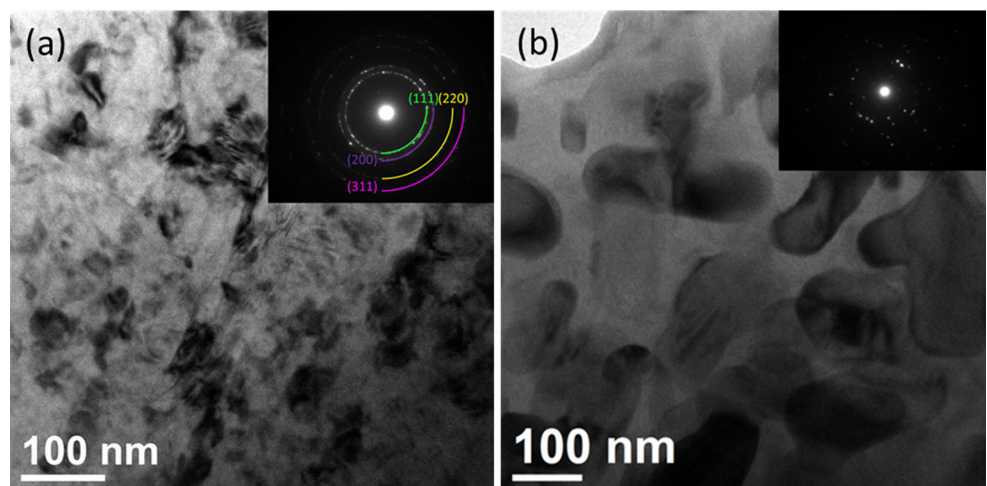


**Figure 2** TEM micrographs of isothermally annealed specimens for annealing temperatures from 200 to 400 °C and annealing times from 30 min to 4 h are shown. The intermetallic phase and

corresponding diffraction spots are marked with green arrows. The as deposited structure is shown at the bottom right for reference.

**Figure 3** **a** A TEM micrograph of a sample annealed at 200 °C ( $\sim 0.5 T_m$  of pure Al) for 1 month. The average grain size remains around 100 nm with no evidence of the second phase intermetallic. **b** A sample annealed at 300 °C ( $\sim 0.6 T_m$  of pure Al) for 1 month where a significant amount of  $Al_6Mn$  formed.



develops at 200 °C after even a month of exposure, further corroborating the lack of phase evolution. This result is noteworthy because at 200 °C, the

nominal solubility limit for Mn in FCC Al is reported to be 0.62 at.% [16], while the present material is beyond that limit by about 6 at.%. We can suggest



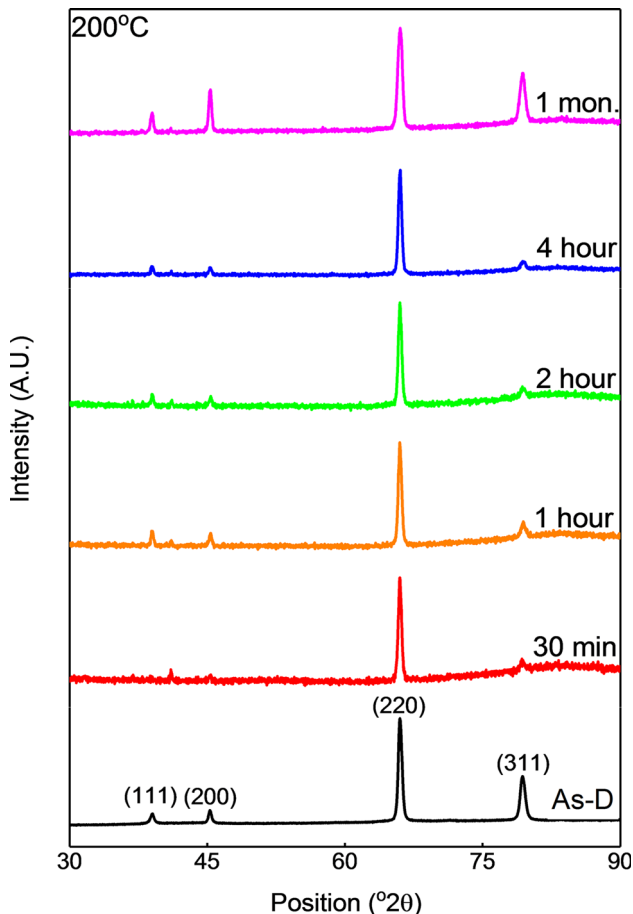


**Figure 4** The XRD patterns for samples annealed at 200 °C for durations from 30 min to 1 month are shown along with the as-deposited (As-D) sample, which is single-phase nanostructured Al-Mn. The expected position of the dominant intermetallic peak is marked with a black diamond.

two contributing reasons that this solution would remain mixed at this temperature (which is about half of the absolute melting point of Al). First, we have recently demonstrated [5] that in the as-deposited condition, this alloy exhibits mild segregation of Mn to the grain boundaries. The combination of a nanoscale grain size (with its increased volume of grain boundary sites) and an apparent preference for solute to occupy those sites can together lead to an apparently increased solubility limit for such nanostructured alloys, [17], as solute can sit in the grain boundary instead of in the FCC lattice. Second, it is possible that the decomposition of the solution is kinetically suppressed over the timescale of months; the kinetics of the transformation are more easily accessed at higher temperatures.

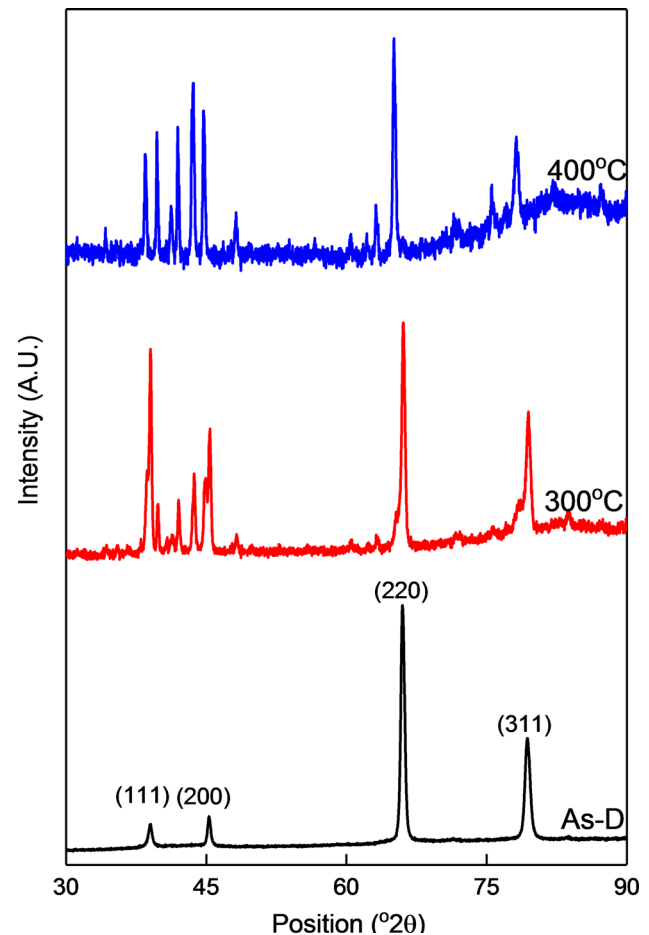


**Figure 5** The XRD patterns of samples annealed at 300 and 400 °C for 30 min, and the as-deposited sample (As-D). The intermetallic forms within 30 minutes at these temperatures.

At higher temperatures, the TEM observations reveal the emergence of second-phase precipitation, as expected at this level of supersaturation. Close inspection of Fig. 2 shows that within 30 min, the samples annealed at 300 and 400 °C already showed precipitates of the intermetallic  $\text{Al}_6\text{Mn}$  phase; some of these are marked with arrows. The XRD patterns of these samples are shown in Fig. 5, revealing more clearly the emergence of the intermetallic phase after 30 min of annealing. Furthermore, the sample annealed at 400 °C exhibits higher intensity peaks, which means that the precipitation of  $\text{Al}_6\text{Mn}$  has occurred more rapidly and the reaction at 300 °C is not complete after 30 min.

Figure 6 shows the grain sizes as a function of time at 200, 300 and 400 °C. The grain size at 300 °C, after a slight relaxation at the earliest annealing time, stabilized at around 110 nm, which is close to the grain

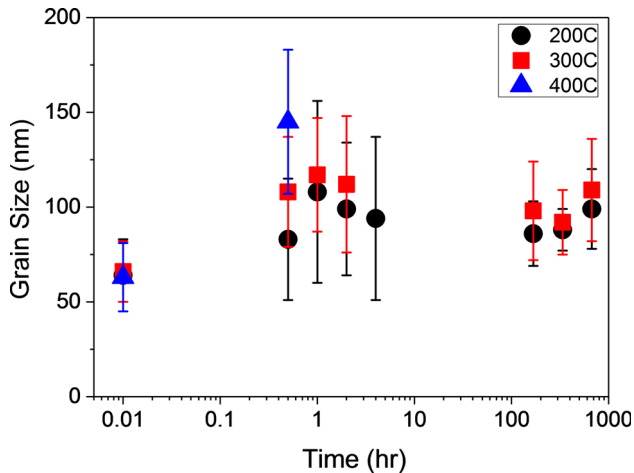


**Figure 6** Grain sizes of the samples annealed at 200, 300 and 400 °C as a function of annealing duration as measured from dark-field TEM images.

size of roughly 100 nm measured in the 200 °C sample after annealing. At 400 °C, the increment of grain growth in the first 30 min of annealing is larger than for the other specimens, with an average grain size of greater than 150 nm. While we did not explore times-at-temperature beyond 30 min for 400 °C, this data point suggests sufficient mobility for the system to be evolving quickly to equilibrium and for grains to continue growing.

The presence of solute and its preference for grain boundary sites in particular is likely responsible for the stability of the grain structure at 200 °C; nanocrystalline pure aluminum at a comparable temperature would have coarsened to the micrometer scale in about an hour [18–21]. Mn atoms in solution should provide kinetic stability through the conventional solute drag mechanism, and solute segregation at grain boundaries also lowers the excess energy of the grain boundaries and the driving force for grain growth [22–27].

Interestingly, at 300 °C, the grain size after 1 month of annealing is roughly unchanged even though precipitation of the  $\text{Al}_6\text{Mn}$  phase has occurred. There are a number of possible reasons for this dual-phase apparently stable nanostructural configuration. First, it is possible that the precipitation reaction has occurred only to a limited degree as compared with what would be expected for a bulk alloy, leaving some solute in the grain boundaries in equilibrium. Alloys in which phase separation is the ground state but grain boundary segregation is the first activated

state (vis-à-vis a solid solution) are referred to as “nano-duplex” [28]. In the case of Al-Mn, the enthalpy of the intermetallic compound is  $-16.7$  kJ/mol [29], the enthalpy of grain boundary segregation is roughly 1.5 kJ/mol [5], and the enthalpy of mixing is  $-102$  kJ/mol [30]; it is therefore reasonable to expect some grain boundary segregation in equilibrium with the second phase at finite temperatures [27, 31]. In this case, the mechanism providing stability at 200 °C, i.e., grain boundary segregation and/or solute drag, is still in effect and is not entirely removed due to the precipitation of the second phase. Second, the formation of second-phase  $\text{Al}_6\text{Mn}$  is also expected to provide grain structural stabilization through Zener pinning. This new mechanism could effectively replace grain boundary segregation as a source of grain size stabilization, especially at lower temperatures where such pinning is kinetically effective.

It is not until the temperature is increased up to 400 °C that the grain boundaries are released. At high enough temperatures, we would expect grain boundary segregation to be lessened, second-phase precipitates to coarsen, and kinetic barriers associated with grain boundaries detaching from either solute or second-phase pinning points to be lowered [32]. It is encouraging that for all of the annealing conditions studied here, grain growth does not appear to be running away as is often seen in unalloyed nanocrystalline materials, and at 200–300 °C the grain size appears to stabilize around 100 nm for a duration of several months.

### Kinetic analysis

Based on the above results, it is clear that during thermal exposure of nanocrystalline Al-6.5 at.% Mn, grain growth is not the principal instability of the system. Rather, phase separation is the first major structural change to occur in these alloys upon heating, and this in turn may play a role in desegregating the grain boundaries and potentially unlocking grain growth. Accordingly, the phase transformation represents the key degradation mechanism, and it is necessary to develop a quantitative picture of its kinetics. We approach this by using a Johnson–Mehl–Avrami–Kolmogorov (JMAK) analysis, which has been used extensively for solid-state precipitation [33–36] and crystallization [37–42]

reactions. The analytical JMAK solution for an isochronal process by Mittemeijer et al. is used here [43–46]. The so-called extensive volume in the JMAK analysis (i.e., the transformed volume without impingement of the transformation product precipitates) can be written as:

$$V_e = \int_0^t V \dot{N}(T(t)) Y(T(t)) d\tau \tag{1}$$

in which  $V$  is the sample volume,  $\dot{N}(T(t))$  is the nucleation rate as a function of time,  $t$ , and temperature,  $T$ , and  $Y(T(t))$  is the time- and temperature-dependent growth rate. The transformation product can only form if there is parent phase left to form it and if there is solute left to feed it. These factors slow the transformation and can be captured using the conventional relationship between the extended volume and the true transformation product volume,  $V_t$ :

$$dV_t = \frac{aV - V_t}{aV} dV_e \tag{2}$$

The parameter  $a$  represents the volume fraction at which the transformation saturates or completes. In the present case, there is not expected to be any impingement of  $Al_6Mn$  precipitates because their equilibrium volume fraction is below  $a = 25\%$  at temperatures ranging from 200 to 400 °C, with specific values at any temperature being easily calculable from the phase diagram [16] using the lever rule; instead, the saturation of the reaction occurs by loss of solute from the matrix.

In what follows below, we will calibrate the parameters of the JMAK analysis using constant heating-rate DSC experiments. For such an isochronal condition, Mittemeijer et al. derive the following JMAK expression (adapted to include the equilibrium volume fraction,  $a$ ) [47]:

$$f = 1 - \exp\left(-\frac{V_e}{aV}\right) = 1 - \exp\left(-\left(\frac{RT^2}{b}\right)^n \frac{k^n}{a} \exp\left(-\frac{nQ}{RT}\right)\right) \tag{3}$$

where  $f = V_t/aV$  is the fraction of the transformation that has occurred at a temperature,  $T$ , given the (constant) heating rate,  $b$ , where  $k$  is a pre-exponential factor accounting for nucleation rate effects,  $n$  is the growth exponent determined by dimensionality and growth mode,  $Q$  is the activation energy, and  $R$  is the gas constant.

The heat released during a DSC scan is proportional to the transformed fraction:

$$\frac{dH}{dT} = \Delta H \frac{df}{dT} \tag{4}$$

in which  $\frac{dH}{dT}$  is the heat flow in the isochronal DSC experiment,  $\Delta H$  is the total heat of transformation, i.e., the total area under the DSC curve after background subtraction to isolate the transformation peak.

Substituting Eq. (3) into Eq. (4), the heat flow during a constant thermal ramp is given as:

$$\frac{dH}{dT} = \Delta H \frac{1}{ab} n k^n (Q + 2RT) \left(\frac{RT^2}{b}\right)^{n-1} \exp\left[\left(\frac{RT^2}{b}\right)^n \frac{k^n}{a} \exp\left(-\frac{nQ}{RT}\right) - \frac{nQ}{RT}\right] \tag{5}$$

The DSC experimental results are shown in Fig. 7 as black solid lines along with the least squares best-fit

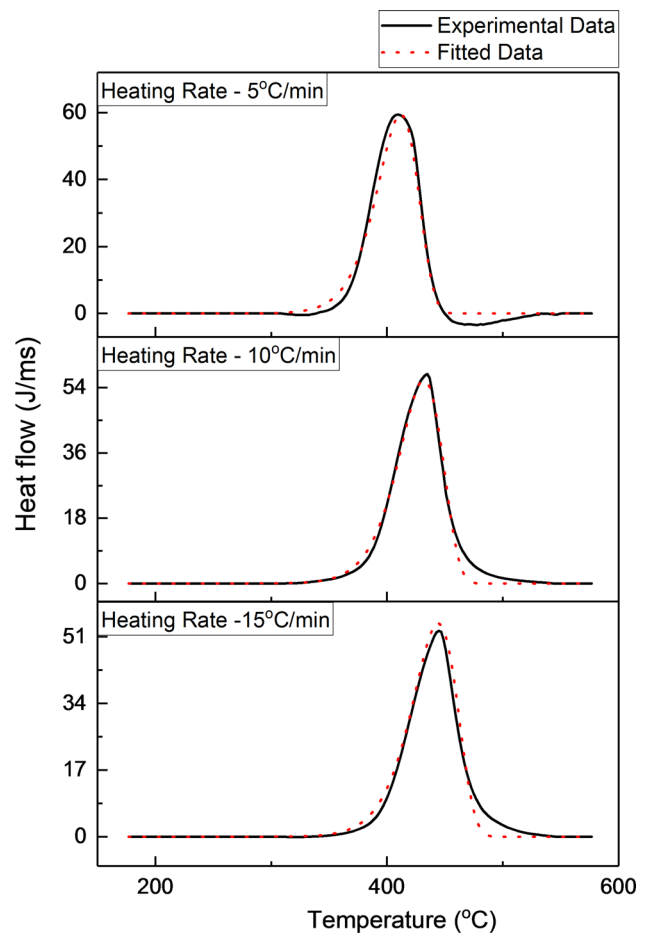


**Figure 7** DSC data of three different ramping rates from 5 to 15 °C/min (solid black line) alongwith the fitted JMAK analytical solution (dashed red line) used to calculate the activation energy, reaction constant, and growth index.

form of Eq. (5), with heating rates from 5 to 15 °C/min. The black lines are the experimental data, and the red dashed best-fit lines achieve a very satisfactory coefficient of determination of  $R^2 = 0.98$ . The fitting here used exactly three unknowns, namely  $k$ ,  $Q$ , and  $n$ , and all of the data sets in Fig. 7 were fitted simultaneously with the same values of these parameters. The fitted reaction constant  $k = 99.2 \text{ s}^{-1}$  is not of immediate physical significance, but the values of  $n$  and  $Q$  are mechanistically important.

First, the activation energy is fitted as  $Q = 126.9 \text{ kJ/mol}$ . In the literature, the precipitation activation energy of  $\text{Al}_6\text{Mn}$  from 3 at.% Al–Mn alloys, Al–Mn–Mg alloys, and 3003 Al alloys were measured between 80 and 167 kJ/mol [48–50]. The present value is quite in line with these values. It is also appropriately lower than the activation energy for bulk diffusion of Mn in FCC Al, which is given as roughly 200 kJ/mol [51], as we expect the nanostructure and excess concentration of Mn at grain boundaries to access short-circuit grain boundary diffusion preferentially during the precipitation reaction.

Second, the fitted value of the kinetic exponent is  $n = 1.6$ , which in the JMAK analysis is defined as [47]

$$n = \frac{d}{m} + c \quad (6)$$

where  $d$  is the dimensionality of the transformation,  $m = 1$  for interface limited growth and 2 for diffusion-controlled growth, and  $c$  is a constant that lies between 0 and 1, suggesting a more or less site saturation nucleation process ( $c = 0$ ) vis-à-vis a continuous nucleation process ( $c = 1$ ). From the volume and condition of the sample, the precipitation of  $\text{Al}_6\text{Mn}$  is a 3-dimensional process, so we may assume that  $d = 3$ . Since  $n$  is measured to be 1.6, we can further conclude that growth is a diffusion-controlled process ( $m = 2$ ) and nucleation is likely site-saturated ( $c = 0.1$ ). These conclusions are eminently reasonable in light of the physics of the process, which involves slow solid-state diffusion to collect solute to the precipitates and starts from grain boundaries that are segregated with solute, with an abundance of viable nucleation sites.

### Isothermal transformation kinetics

The above experiments were all based on a constant thermal scan rate in DSC, but they calibrate the kinetic model for the transformation more generally.

With the resulting fitting parameters, a conventional isothermal time–temperature–transformation (TTT) diagram can be constructed for the  $\text{Al}_6\text{Mn}$  precipitation reaction using Eq. (3). This construction requires that the isochronal transformation data be converted to isothermal data, which can be accomplished using the inverse additive rule [52]:

$$\tau(f, T) = \left( \frac{dT}{db} \right)_f \quad (7)$$

where  $\tau(f, T)$  is the time to reach a fraction transformed,  $f$ , at temperature,  $T$ , which can be determined from the derivative of the temperature (at which the same fraction transformed would be reached isochronally) with respect to the heating rate. This derivative is performed numerically on Eq. (3) using the fitted parameters.

The resulting TTT diagram is shown in Fig. 8, with contour lines for 1, 50 and 99% transformed states. The TTT diagram derived from the isochronal experiments compares reasonably well with the independent experimental results based on isothermal annealing. In the TTT diagram, the reaction begins at roughly 30 s and completes after about 45 min at 400 °C, which is roughly in line with the

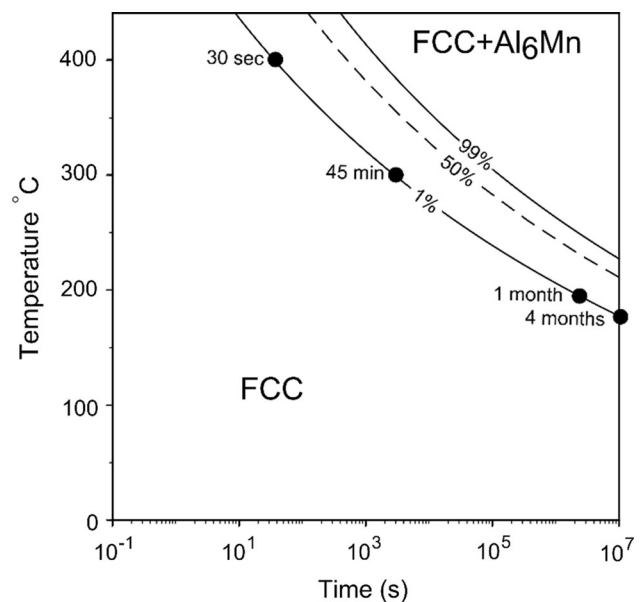


**Figure 8** The TTT diagram constructed using the parameters acquired from the DSC fitting in Fig. 7. According to the TTT diagram at 400 °C the intermetallic formation starts within 30 min and at 200 °C the system is free from transformation for roughly 1 month which is in line with experiments.



observation of intermetallics after 30 min in the isothermal experiment (see Figs. 2 and 5). At 200 °C ( $T = 0.5 T_m$ ), it was experimentally observed that no transformation occurred after 1 month, which is on the same order of magnitude as the time predicted in the TTT diagram for the transformation to begin (roughly 27 days). The TTT diagram seems to slightly overestimate the time required to start the transformation at 300 °C and slightly underestimate the time at 200 °C, which is a result of using the fitted form of Eq. (3) at heating rates outside of the 5–15 °C/min window, but still provides a reasonably accurate result. The strong correspondence between the kinetics attained from DSC and observations from microscopy suggests that the TEM microstructures are representative of the overall film.

This TTT diagram can serve as a general guideline for heat treatment processes. For example, a rapid thermal excursion at 300 °C without transformation is possible for post-processing operations such as soldering. It also suggests that the alloy can have a reasonable stable service lifetime at temperatures below 200 °C, which is of practical engineering use. Interestingly, the time-to-transformation increases dramatically below 200 °C, growing to 4 months at 175 °C.

## Conclusion

In conclusion, the nanostructure evolution for Al-6.5 at.% Mn, including grain growth and phase transformation, was explored. The alloy is a single-phase solid-solution alloy with a grain size of approximately 65 nm in the as-deposited condition, with Mn segregated at grain boundaries and a supersaturation of Mn in the grains. Whereas grain growth is generally suppressed in the solid-solution phase, the phase separation that produces Al<sub>6</sub>Mn is the principal instability in this system. Grain growth is restrained to average grain sizes of roughly 100 nm up to 300 °C even after 1 month of annealing.

By studying the Al<sub>6</sub>Mn precipitation reaction using isochronal differential scanning calorimetry, we evaluate the JMAK parameters underlying the phase transformation. The resulting kinetics are consistent with a three-dimensional diffusion-controlled process with an activation energy of 127 kJ/mol, which is reasonable in light of prior work on the same reaction in other (non-nanocrystalline) alloys in this family. These transformation kinetics allowed for the

construction of a conventional isothermal TTT diagram across a large temperature and time range. Through extended isothermal annealing experiments, the TTT diagram was verified to be reasonably predictive. Experimentally at 200 °C, which is one-half of the melting temperature of Al, the alloy can retain its nanostructure over a month of annealing, without significant formation of intermetallic phases. The TTT diagram further predicts that the alloy can sustain longer annealing times for at least several months without formation of intermetallics at 175 °C, which makes the alloy amenable to some downstream engineering processes such as soldering and possibly for extended use at modest elevated temperatures.

## Acknowledgements

This research was supported (in part) by the U.S. Army Research Office under contract W911NF-13-D-0001 through the Institute of Soldier Nanotechnologies at MIT. A.R.K would like to thank the Department of Defense for support through the National Defense Science and Engineering Fellowship.

## References

- [1] Suryanarayana C, Sundaresan R (1991) Metastable phases in mechanically alloyed Al-Mn powder mixtures. *Mater Sci Eng, A* 131:237–242
- [2] Nam SW, Lee DH (2000) The effect of Mn on the mechanical behavior of Al alloys. *Met Mater Int* 6(1):13–16
- [3] Cai W, Schuh CA (2012) Tuning nanoscale grain size distribution in multilayered Al-Mn alloys. *Scr Mater* 66:194–197. <https://doi.org/10.1016/j.scriptamat.2011.10.040>
- [4] Ruan S, Schuh CA (2009) Electrodeposited Al-Mn alloys with microcrystalline, nanocrystalline, amorphous and nano-quasicrystalline structures. *Acta Mater* 57(13):3810–3822. <https://doi.org/10.1016/j.actamat.2009.04.030>
- [5] Huang T-Y, Marvel CJ, Cantwell PR, Harmer MP, Schuh CA (2016) Grain boundary segregation in Al-Mn electrodeposits prepared from ionic liquid. *J Mater Sci* 51(1):438–488. <https://doi.org/10.1007/s10853-015-9316-2>
- [6] Ruan S, Schuh CA (2012) Towards electroformed nanostructured aluminum alloys with high strength and ductility. *J Mater Res* 27(12):1638–1651. <https://doi.org/10.1557/jmr.2012.105>
- [7] McGeough JA, Leu MC, Rajurkar KP, De Silva AKM, Liu Q (2001) Electroforming process and application to

- micro/macro manufacturing. *CIRP Ann Manuf Technol* 50(2):499–514. [https://doi.org/10.1016/S0007-8506\(07\)62990-4](https://doi.org/10.1016/S0007-8506(07)62990-4)
- [8] Dini JW (1993) *Electrodeposition—the materials science of coatings and substrates*. William Andrew Publishing, Noyes
- [9] Talin AA, Marquis EA, Goods SH, Kelly JJ, Miller MK (2006) Thermal stability of Ni–Mn electrodeposits. *Acta Mater* 54(7):1935–1947. <https://doi.org/10.1016/j.actamat.2005.12.027>
- [10] Chookajorn T, Murdoch HA, Schuh CA (2012) Design of stable nanocrystalline alloys. *Science* 337(6097):951–954. <https://doi.org/10.1126/science.1224737>
- [11] Zahid GH, Huang Y, Prangnell PB (2009) Microstructure and texture evolution during annealing a cryogenic-SPD processed Al-alloy with a nanoscale lamellar HAGB grain structure. *Acta Mater* 57(12):3509–3521. <https://doi.org/10.1016/j.actamat.2009.04.010>
- [12] Rupert TJ, Trelewicz JR, Schuh CA (2012) Grain boundary relaxation strengthening of nanocrystalline Ni–W alloys. *J Mater Res* 27(09):1285–1294. <https://doi.org/10.1557/jmr.2012.55>
- [13] Detor AJ, Schuh CA (2011) Microstructural evolution during the heat treatment of nanocrystalline alloys. *J Mater Res* 22(11):3233–3248. <https://doi.org/10.1557/JMR.2007.0403>
- [14] Boylan K, Ostrander D, Erb U, Palumbo G, Aust KTT (1991) An in-situ TEM study of the thermal stability of nanocrystalline NiP. *Scr Metall Mater* 25(1):2711–2716
- [15] Färber B, Cadel E, Menand A, Schmitz G, Kirchheim R (2000) Phosphorus segregation in nanocrystalline Ni–3.6 at.% P alloy investigated with the tomographic atom probe (TAP). *Acta Mater* 48:789–796
- [16] McAlister AJ, Murray JL (1987) The (Al–Mn) Aluminum–Manganese system. *J Phase Equilib* 8(5):438–447. <https://doi.org/10.1007/BF02893153>
- [17] Chookajorn T, Park M, Schuh CA (2015) Duplex nanocrystalline alloys: entropic nanostructure stabilization and a case study on W–Cr. *J Mater Res* 30(02):151–163. <https://doi.org/10.1557/jmr.2014.385>
- [18] Manna R, Mukhopadhyay NK, Sastry GVS (2008) Effect of equal channel angular pressing on microstructure and mechanical properties of commercial purity aluminum. *Metall Mater Trans A* 39:1525–1534. <https://doi.org/10.1007/s11661-007-9419-8>
- [19] Abdoli H, Ghanbari M, Baghshahi S (2011) Thermal stability of nanostructured aluminum powder synthesized by high-energy milling. *Mater Sci Eng, A* 528(22–23):6702–6707. <https://doi.org/10.1016/j.msea.2011.05.057>
- [20] Legros M, Gianola DS, Hemker KJ (2008) In situ TEM observations of fast grain-boundary motion in stressed nanocrystalline aluminum films. *Acta Mater* 56(14):3380–3393. <https://doi.org/10.1016/j.actamat.2008.03.032>
- [21] Ferry M, Hamilton NE, Humphreys FJ (2005) Continuous and discontinuous grain coarsening in a fine-grained particle-containing Al–Sc alloy. *Acta Mater* 53(4):1097–1109. <https://doi.org/10.1016/j.actamat.2004.11.006>
- [22] Kim SG, Park YB (2008) Grain boundary segregation, solute drag and abnormal grain growth. *Acta Mater* 56(15):3739–3753. <https://doi.org/10.1016/j.actamat.2008.04.007>
- [23] Trelewicz J, Schuh C (2009) Grain boundary segregation and thermodynamically stable binary nanocrystalline alloys. *Phys Rev B* 79(9):1–13. <https://doi.org/10.1103/PhysRevB.79.094112>
- [24] Liu F, Kirchheim R (2004) Nano-scale grain growth inhibited by reducing grain boundary energy through solute segregation. *J Cryst Growth* 264:385–391. <https://doi.org/10.1016/j.jcrysgro.2003.12.021>
- [25] Raabe D, Herbig M, Sandlöbes S, Li Y, Tytko D, Kuzmina M, Ponge D, Choi PP (2014) Grain boundary segregation engineering in metallic alloys: a pathway to the design of interfaces. *Curr Opin Solid State Mater Sci* 18(4):253–261. <https://doi.org/10.1016/j.cossms.2014.06.002>
- [26] Kirchheim R (2007) Reducing grain boundary, dislocation line and vacancy formation energies by solute segregation. I. Theoretical background. *Acta Mater* 55(15):5129–5138. <https://doi.org/10.1016/j.actamat.2007.05.047>
- [27] Chookajorn T, Schuh CA (2014) Thermodynamics of stable nanocrystalline alloys: a Monte Carlo analysis. *Phys Rev B* 89(6):064102. <https://doi.org/10.1103/PhysRevB.89.064102>
- [28] Chookajorn T, Park M, Schuh CA (2015) Duplex nanocrystalline alloys: entropic nanostructure stabilization and a case study on W–Cr. *J Mater Res* 30(May):151
- [29] Saal JE, Kirklin S, Aykol M, Meredig B, Wolverton C (2013) Materials design and discovery with high-throughput density functional theory: the Open Quantum Materials Database (OQMD). *JOM* 65(11):1501–1509. <https://doi.org/10.1007/s11837-013-0755-4>
- [30] Murdoch HA, Schuh CA (2013) Estimation of grain boundary segregation enthalpy and its role in stable nanocrystalline alloy design. *J Mater Res* 28(16):2154–2163. <https://doi.org/10.1557/jmr.2013.211>
- [31] Kalidindi AR, Schuh CA (2017) Stability criteria for nanocrystalline alloys. *Acta Mater* 132:128–137. <https://doi.org/10.1016/j.actamat.2017.03.029>
- [32] Kalidindi AR, Schuh CA (2017) Phase transitions in stable nanocrystalline alloys. *J Mater Res* 32(11):1993–2002. <https://doi.org/10.1557/jmr.2017.188>

- [33] Starink MJ (2001) On the meaning of the impingement parameter in kinetic equations for nucleation and growth reactions. *J Mater Sci* 36(18):4433–4441. <https://doi.org/10.1023/A:1017974517877>
- [34] Starink MJ (1997) Kinetic equations for diffusion-controlled precipitation reactions. *J Mater Sci* 2:4061–4070. <https://doi.org/10.1023/A:1018649823542>
- [35] Starink MJ, Zahra A-MM (1998) Kinetics of isothermal and non-isothermal precipitation in an Al-6 at.% Si alloy. *Philos Mag A* 77(1):187–199. <https://doi.org/10.1080/01418619808214237>
- [36] Kempen ATW, Sommer F, Mittemeijer EJ (2002) The isothermal and isochronal kinetics of the crystallisation of bulk amorphous Pd<sub>40</sub>Cu<sub>30</sub>P<sub>20</sub>Ni<sub>10</sub>. *Acta Mater* 50(6):1319–1329. [https://doi.org/10.1016/S1359-6454\(01\)00428-1](https://doi.org/10.1016/S1359-6454(01)00428-1)
- [37] Ruitenberg G, Petford-Long AK, Doole RC (2002) Determination of the isothermal nucleation and growth parameters for the crystallization of thin Ge<sub>2</sub>Sb<sub>2</sub>Te<sub>5</sub> films. *J Appl Phys* 92(6):3116. <https://doi.org/10.1063/1.1503166>
- [38] Rheingans B, Mittemeijer EJ (2013) Phase transformation kinetics: advanced modeling strategies. *JOM* 65(9):1145–1154. <https://doi.org/10.1007/s11837-013-0674-4>
- [39] Hu DZ, Lu XM, Zhu JS, Yan F (2007) Study on the crystallization by an electrical resistance measurement in Ge<sub>2</sub>Sb<sub>2</sub>Te<sub>5</sub> and N-doped Ge<sub>2</sub>Sb<sub>2</sub>Te<sub>5</sub> films. *J Appl Phys* 102(11):113507. <https://doi.org/10.1063/1.2818104>
- [40] Kelton KF, Croat TK, Gangopadhyay AK, Xing L-Q, Greer AL, Weyland M, Li X, Rajan K (2003) Mechanisms for nanocrystal formation in metallic glasses. *J Non Cryst Solids* 317(1–2):71–77. [https://doi.org/10.1016/S0022-3093\(02\)02004-5](https://doi.org/10.1016/S0022-3093(02)02004-5)
- [41] Greer ALL (1994) Crystallization of metallic glasses. *Mater Sci Eng, A* 179–180:41–45. [https://doi.org/10.1016/0921-5093\(94\)90161-9](https://doi.org/10.1016/0921-5093(94)90161-9)
- [42] Chen LCC, Spaepen F (1991) How to use calorimetry to distinguish a microcrystalline structure from an amorphous structure. *Mater Sci Eng, A* 133:342–345. [https://doi.org/10.1016/0921-5093\(91\)90084-Z](https://doi.org/10.1016/0921-5093(91)90084-Z)
- [43] Liu F, Sommer F, Mittemeijer EJ (2011) Parameter determination of an analytical model for phase transformation kinetics: application to crystallization of amorphous Mg–Ni alloys. *J Mater Res* 19(09):2586–2596. <https://doi.org/10.1557/JMR.2004.0341>
- [44] Nitsche H, Sommer F, Mittemeijer EJ (2005) The Al nanocrystallization process in amorphous Al<sub>85</sub>Ni<sub>8</sub>Y<sub>5</sub>Co<sub>2</sub>. *J Non Cryst Solids* 351(49–51):3760–3771. <https://doi.org/10.1016/j.jnoncrysol.2005.08.040>
- [45] Liu F, Sommer F, Mittemeijer EJ (2004) Determination of nucleation and growth mechanisms of the crystallization of amorphous alloys; application to calorimetric data. *Acta Mater* 52(11):3207–3216. <https://doi.org/10.1016/j.actamat.2004.03.020>
- [46] Mittemeijer E (1992) Analysis of the kinetics of phase transformations. *J Mater Sci* 27:3977–3987. <https://doi.org/10.1007/BF01105093>
- [47] Liu F, Sommer F, Bos C, Mittemeijer EJ (2007) Analysis of solid state phase transformation kinetics: models and recipes. *Int Mater Rev* 52(4):193–212. <https://doi.org/10.1179/174328007X160308>
- [48] Ciavaguera N, Diego JA, Clavaguera-Mora MT, Inoue A (1995) Nanocrystalline formation of AlNiNdCu materials: a kinetic study. *Nanostructured Mater* 6(95):485–488
- [49] Agreda NJ, Luiggi J (2005) Isochronal study of Al–Mg, Al–Mn, and Al–Mn–Mg alloys using electrical resistivity and thermoelectric power. *Mater Res*. <https://doi.org/10.1590/S1516-14392005000100007>
- [50] Luiggi NJ (1997) Isothermal precipitation of commercial 3003 Al alloys studied by thermoelectric power. *Metall Mater Trans B* 28(February):125–133
- [51] Du Y, Chang Y, Huang B, Gong W, Jin Z, Xu H, Yuan Z, Liu Y, He Y, Xie F-Y (2003) Diffusion coefficients of some solutes in fcc and liquid Al: critical evaluation and correlation. *Mater Sci Eng, A* 363(1–2):140–151. [https://doi.org/10.1016/S0921-5093\(03\)00624-5](https://doi.org/10.1016/S0921-5093(03)00624-5)
- [52] Rios PR (2005) Relationship between non-isothermal transformation curves and isothermal and non-isothermal kinetics. *Acta Mater* 53(18):4893–4901. <https://doi.org/10.1016/j.actamat.2005.07.005>